Hard X-ray and γ-ray spectroscopy at high temperatures using a COTS SiC photodiode

Article (Accepted Version)

Hard X-ray and γ-ray spectroscopy at high temperatures using a COTS SiC photodiode

C.S. Bodie*, G. Lioliou, A.M. Barnett
Space Research Group, Sch. of Mathematical and Physical Sciences, University of Sussex, Falmer, Brighton, BN1 9QT, UK
* *Corresponding Author, Tel: +44 1273 873982, Email: c.bodie@sussex.ac.uk*

Abstract

A commercial-off-the-shelf (COTS) silicon carbide (4H-SiC) UV photodiode was electrically characterized and investigated as a low-cost spectroscopic photon counting detector of X-rays and γ-rays. The detector was coupled to a custom-built low-noise charge-sensitive preamplifier, and illuminated by ^{55}Fe and ^{109}Cd radioisotope X-ray sources and an ^{241}Am radioisotope γ-ray source, thus providing photon energies from 5.9 keV to 59.5 keV. The detector and preamplifier were operated uncooled at temperatures between 20 °C and 100 °C. The energy resolution (full width at half maximum, *FWHM*) of the spectrometer was found to be 1.66 keV ± 0.15 keV at 5.9 keV and 22.16 keV, and 1.83 keV ± 0.15 keV at 59.5 keV when operated at 20 °C. At a temperature of 100 °C, the *FWHM* were 2.69 ± 0.25 keV, 2.65 keV± 0.25 keV, and 3.30 keV ± 0.30 keV, at the same energies. Shaping time noise analysis found dielectric noise to be the dominant noise source, except when long amplifier shaping times were used at high temperatures when white parallel noise dominated. Noise associated with incomplete charge collection was found to be negligible at energies up to 22.16 keV and at temperatures ≤ 60 °C; but incomplete charge collection noise could not be discounted when the spectrometer was operated at higher temperature (80 °C) and at higher energy (59.5 keV). Although the detector was thin (and thus inefficient at high photon energies) the low cost and commercial availability of the SiC device make it an attractive prospect for use in cost-sensitive applications such as university-led CubeSat missions.

1. Introduction

Many semiconductor materials have been investigated for use as photodiodes for photon counting X-ray spectrometers. However, Si with its bandgap, E_g, of 1.12 eV [1], remains the gold standard spectroscopic X-ray photodiode material for use at relatively cool temperatures (≤ 20 °C) [2]. Because of its relatively narrow bandgap, Si radiation detectors typically require cooling to limit the thermally generated leakage current that can degrade the energy resolution of an X-ray spectrometer [3]. Radiation shielding is another common prerequisite for spectroscopic Si detectors sited in environments of high energy radiation, e.g. space [4]; radiation damage to Si detectors can be sufficient to cause substantial degradation in performance, even in the relatively benign Earth-Moon environment [5]. As such, significant research attention has been paid to developing alternative semiconductor materials for photon counting radiation spectroscopy, particularly with future space science applications in mind. GaAs [6] (E_g = 1.42 eV [7]), CdZnTe [8] (E_g = 1.54 eV [9]), $Al_{0.8}Ga_{0.2}As$ [10](E_g = 2.09 eV [11]), 4H-SiC [12] (E_g = 3.27 eV [13]), and Diamond (E_g = 5.47 eV [14, 15]), are among many wide bandgap semiconductors that are considered to be intrinsically more radiation tolerant than Si in most circumstances, and with the exception of diamond, these materials have been shown to be capable of spectroscopic X-ray response at elevated temperatures (≥ 20 °C). It is the goal of developing solid state soft X-ray radiation detectors that do not require cooling and radiation shielding that has driven much recent research into wide bandgap materials for X-ray spectrometry [12]. It should also be noted that many (e.g. GaAs, AlGaAs, CdZnTe), but not all (e.g. SiC, Diamond), wide bandgap materials also have larger X-ray/γ-ray linear absorption coefficients than Si. As such, their development has also been motivated by the need for better quantum detection efficiency at hard photon energies [16].

Bertuccio et al. first reported spectroscopic X-ray detection with epitaxial 4H-SiC [17]. An epitaxial 4H-SiC Schottky diode detector was used with appropriate readout electronics to accumulate an ^{241}Am X-ray and γ-ray spectrum, with the Np L X-ray photopeaks at 13.9 keV and 17.8 keV resolved clearly. Later work reported SiC devices operating at temperatures up to 100 °C [18] where an equivalent noise charge (ENC) of 44 e^- rms on a pulser line at 100 °C was achieved. The best photon counting X-ray

spectroscopic results obtained with 4H-SiC to date showed an ENC of 10.6 e^- rms (196 eV (full width at half maximum, *FWHM*) at 30 °C increasing to 12.7 e^- rms (233 eV *FWHM*) at 100 °C [19], on an ^{55}Fe Kα emission line (5.9 keV). Those results represent the cutting edge of SiC radiation detector development using the highest purity materials and with the detectors connected to state-of-the-art CMOS preamplifiers. Alongside demand for these state-of-the-art devices in major space missions, there is also demand for lower cost X-ray spectrometers for machine condition monitoring [20], marine exploration and engineering [21], and low-cost CubeSat space missions.

The temperatures experienced by science instrumentation on-board small satellites can vary widely, depending on the thermal design of the spacecraft and its mission. The designers of small satellites strive to keep thermal ranges within those at which commercial off the shelf (COTS) components are rated, and can typically achieve modest (10 °C – 30 °C) temperatures in the interior of the spacecraft using passive thermal management. However, external surfaces where radiation detectors would be located can experience much greater temperature ranges (typically swings of up to 100 °C) [22]. As such, this detector, and the preamplifier to which it was coupled, were investigated at temperatures up to 100 °C.

The work of Terry et al. [23], provided early indication that commercial off the shelf (COTS) SiC photodiodes could be used as detectors for X-ray spectrometers. That work presented the X-ray responsivity of COTS UV diodes up to 6.5 keV. Later work compared the responsivity of the thin COTS SiC UV detectors with thicker (50 μm) purpose grown (not COTS) 4H-SiC X-ray detectors [24]; the purpose grown X-ray detector was spectroscopic to X-rays and achieved an ENC of 73 e^- rms (1.2 keV *FWHM*) at 28 °C at 59.5 keV the highest energy γ-ray emission line from ^{241}Am [25].

Recent work has shown that a commercial-off-the-shelf (COTS) SiC ultraviolet (UV) photodiode could be repurposed as a spectroscopic soft X-ray detector, and even operated at elevated temperatures (≤ 100 °C) when connected to suitable preamplifier electronics [26 - 28]. Here, new results are presented for a photodiode of the same type (area of 0.06 mm^2). The results extend the energy range used to characterize this type of detector. The detector was operated as a spectroscopic photon counting detector of X-ray and γ-ray photons of energies from 5.9 keV to 59.5 keV, across a temperature range of 20 °C to 100 °C.

2. Detector properties

The 4H-SiC detector used in this investigation was a randomly selected COTS UV p-n photodiode of geometry similar to that described by Prasai et al. [29] and made by SG Lux GmbH, Berlin, Germany. The photodiode had an active area of 0.06 mm^2. The thickness of its n-type and p-type layers were 5 μm and 0.15 μm, respectively. The stated net donor and net acceptor concentrations were N_D-N_A = 8 × 10^{15} cm^{-3} and N_A-N_D = 6 × 10^{18} cm^{-3} [29]. The photodiode was purchased from a standard electronic components retailer. It was supplied packaged in a TO-18 can with a UV window. The UV window was removed prior to characterization so that the photodiode could be illuminated directly by X-rays and γ-rays.

3. Experiments and results

3.1 Leakage current measurements

The SiC photodiode was placed in a custom-built electromagnetically-screened, and light-tight test harness located within a TAS Micro MT Climatic cabinet, and connected to a Keithley 6487 picoammeter/voltage source. The test harness was purged with dry N_2 (< 5% relative humidity) before being sealed. Once the test harness was sealed, the climatic cabinet was continually purged with dry N_2 to ensure a dry environment and mitigate against any effects of humidity [10]. National Instruments LabVIEW software was used to automate the measurements. Leakage current as a function of reverse bias was measured at temperatures from 100 °C to 20 °C, in 20 °C intervals. To ensure that the SiC detector was at thermal equilibrium in the test harness during each measurement, 30 minutes waiting time was allowed at each test temperature before the bias was applied and the measurement made. The detector was reverse biased in 1 V increments up to

a maximum of 175 V. The results are presented in Fig. 1, where the diode's leakage current (including leakage current of the detector's packaging) is shown as a function of applied reverse bias. The maximum leakage current recorded was 78.4 pA ± 0.6 pA at 175 V reverse bias and 100 °C. The leakage current at 175 V and 60 °C was 2.1 pA ± 0.4 pA. At temperatures of 40 °C and below, the leakage current was within the noise floor of the picoammeter (± 0.4 pA) at all investigated reverse biases. At 100 V reverse bias, the leakage current was 42.7 pA ± 0.5 pA at 100 °C, and 1.1 pA ± 0.4 pA at 60 °C. As it is useful to compare these results with previous reports in the literature; leakage current densities were also considered. At 100 °C and at 60 °C respectively, the leakage current densities were 71.2 nA cm^{-2} ± 0.8 nA cm^{-2} and 1.8 nA cm^{-2} ± 0.7 nA cm^{-2}, respectively. These leakage current densities were greater than those reported by Bertuccio et al. [12] where current densities of around 1 nA cm^{-2} were reported at 100 °C, at field strengths of 53 kV cm^{-1} and 103 kV cm^{-1}. At 104 kV cm^{-1} the COTS UV SiC photodiode had a leakage current density of 8.4 nA cm^{-2} ± 0.7 nA cm^{-2}, similar to that reported by Zhao et al. [26] for a similar device from the same manufacturer (7.9 nA cm^{-2} ± 0.7 nA cm^{-2} at 101 kV cm^{-1}).

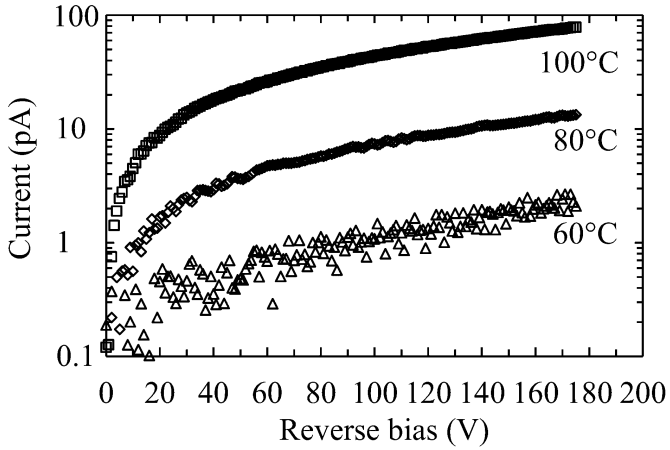

Fig. 1. The SiC detector's leakage current as a function of reverse bias voltage; 100 °C (open squares), 80 °C (open diamonds), and 60 °C (open triangles). The uncertainties (± 0.4 pA to ± 0.6 pA) associated with the leakage current measurements have been omitted for clarity.

3.2 Capacitance measurements

The capacitance of the detector was measured as a function of reverse bias and temperature. The photodiode was placed in another test harness, purged with dry N_2, and subjected to the same environmental regime in the same TAS Micro MT Climatic cabinet as had been used for the leakage current measurements. Capacitance measurements were recorded as a function of reverse bias from 0 V to 175 V, increasing in 1 V steps. Measurements were made from a temperature of 100 °C to 20 °C, in decrements of 20 °C. An HP 4275A multi frequency LCR meter, with a test signal of 50 mV rms magnitude and 1 MHz frequency, was used to measure the photodiode's capacitance as a function of applied reverse bias. The LCR meter was subject to an "open and short" correction in accordance with the manufacturers recommended procedure before measurement was commenced. LabVIEW software was used to automate the process.

The detector's package and the bare-die detector each introduced capacitance when the assembly was reverse biased. The majority of package capacitance originated from the borosilicate glass insulation that insulated the TO package's isolated pin from the rest of the package. Other sources of stray capacitance included the silver loaded epoxy used to die attach the detector to the package. As the detector was wire-bonded to its package in parallel with the packaging capacitance, a capacitance measurement of the packaged detector was followed by a capacitance measurement of a similarly prepared package with the detector's wire-bonds removed. The capacitance of the packaged detector with bond-wires removed was subtracted from the capacitance of the detector with wire-bonds intact to estimate the capacitance of the detector's depleted width. The apparent depletion width was then calculated. The apparent depletion width

as a function of applied reverse bias, $W(V_R)$, was calculated assuming the diode may be approximated as a parallel plate capacitor [30], such that

$$W(V_R) = \frac{\varepsilon_0 \varepsilon A}{C_{DL}(V_R)} \quad (1)$$

where $C_{DL}(V_R)$ is the measured capacitance of the depletion layer, ε_0 is the permittivity of free space, ε is the relative permittivity/dielectric constant, and A is the effective area of the device. The diode's capacitance (with packaging capacitance subtracted) and its calculated apparent depletion width as a function of reverse bias at 100 °C and 20 °C are presented in Fig. 2. The calculated depletion width of the detector at 100 V reverse bias was 2.47 µm ± 0.04 µm and 2.41 µm ± 0.03 µm at 100 °C and 20 °C, respectively. Within the uncertainties of the measurements, the apparent depletion width did not vary over the temperatures investigated. Despite an epitaxial layer width of 5.15 µm [29], at face value the capacitance measurements suggest that only a portion of the epitaxial layer was depleted, reaching a maximum of 2.41 µm ± 0.03 µm at 100 V reverse bias. Given the manufacturer stated donor concentration (8×10^{15} cm^{-3}) [29] and the abrupt junction approximation [30], a depletion width of 3.7 µm at 100 V would have been expected, although no uncertainty in the concentration was stated by the manufacturer. However, despite the depletion region seemingly being only a portion of the epitaxial layer thickness, results previously reported for a detector of the same type (but in that case used as an electron spectrometer [31]) suggested that the entire epitaxial width of the detector was active for radiation detection. It is possible that a significant portion of the epitaxial layer was not depleted and that despite this the whole of the epitaxial layer contributed to the detected signal since the electron and hole recombination lengths in N_D-N_A = 8×10^{15} cm^{-3} n-type and N_A-N_D = 6×10^{18} cm^{-3} p-type doped SiC are ≈ 1.1 µm [32] and ≈ 20 µm [33] respectively. Nevertheless, care should be taken in interpreting the capacitance measurements since they were made using packaged devices rather than bare dice. Furthermore, the computation of the depletion width from measurements relies on approximation of the detector to a parallel plate capacitor. The sensitivity of the measurements to additional capacitances is also noted; an unaccounted 1.87 pF capacitance in series with the detector would result in a detector of capacitance ≈ 1 pF (i.e. depletion width of ≈ 5 µm) appearing to have the capacitance characteristics measured above. The reason for the discrepancy in depletion width between the measurement of capacitance as a function of reverse bias, the doping density calculation, and the epitaxial layer thickness are unknown. However, given that the electron spectroscopy measurements of Zhao et al. [31] indicated that the whole of the epitaxial thickness was active, the full thickness of the epitaxial layer (5.15 µm) was assumed to be active and depleted for the quantum detection efficiency calculation below. Nevertheless, the simplicity of this assumption is recognized. Other effects may also reduce the active layer thickness of the detector; for example, if the detector had a recombination region close to the contact (as has been measured in other X-ray photodiodes [34]) this would reduce the thickness of the active layer, and the quantum detection efficiency of the device would be reduced both as a consequence of the reduction in active layer thickness and because of the introduction of a dead layer ahead of the active layer.

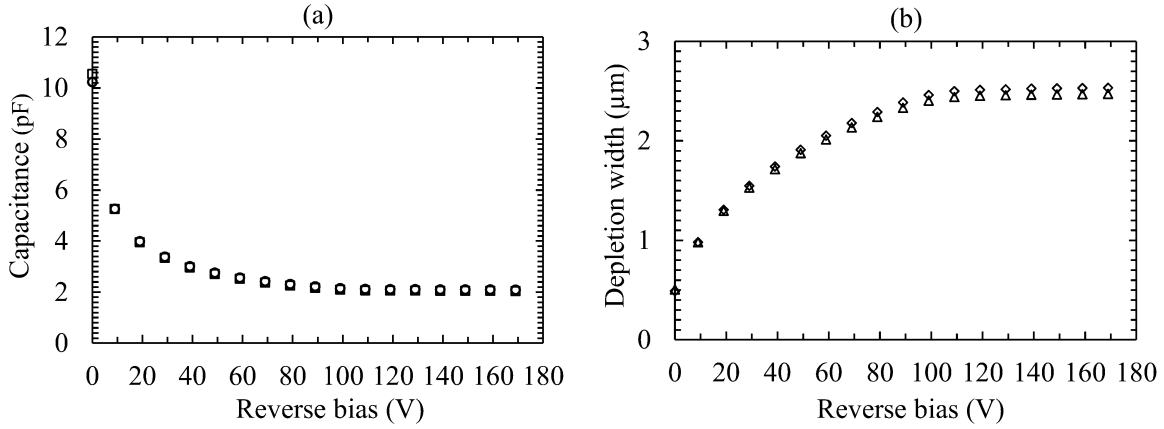

Fig. 2. a) The SiC diode's capacitance at 100 °C (open squares) and 20 °C (open circles) as a function of applied detector reverse bias; b) the apparent depletion width implied by the measured capacitances at 100 °C (open diamonds) and 20 °C (open triangles) as a function of reverse bias. Error bars are omitted for clarity; at 100 V depletion width errors were 0.04 μm and 0.03 μm at 100 °C and 20 °C respectively.

Assuming a 5.15 μm active region thickness, the quantum detection efficiency, *QE*, of the detector from 1 keV to 60 keV was calculated using the Beer-Lambert-Bouguer Law for light attenuation and absorption,

$$QE = \prod_{i=1}^{i=n} \exp\left(\mu_i \rho_i t_i\right)\left(1 - \exp\left(\mu_{en}\rho t\right)\right), \quad (2)$$

where μ_i is the mass attenuation coefficient of inactive layers before the detecting medium, ρ_i is layer density, t_i is layer thickness, μ_{en} is the mass absorption coefficient of the detecting medium, ρ is its density, and t is thickness of the detector's active layer [35]. Mass absorption and attenuation coefficients were obtained from the NIST XCOM database [36].

The calculated quantum detection efficiency of the SiC detector is presented in Fig. 3; the discontinuity shown at 1.8 keV is the Si K absorption edge. The SiC material and the thickness of the diode's active layer, limited the *QE* of the photodiode. Si and C have relatively low linear attenuation coefficients when compared with other compound wide band-gap detectors. The *QE* of the energies of specific interest for the results reported presently were 0.167 at 5.9 keV, 3.52×10^{-3} at 22.16 keV, and 1.56×10^{-4} at 59.5 keV. To compare, the *QE* of a GaAs detector of equal thickness would have been 0.349, 8.26×10^{-2}, and 5.02×10^{-3} at the same photon energies. It should be noted that the quantum detection efficiency calculations did not account for any carrier recombination region close to the front contact of the detector, which would have reduced the quantum detection efficiency of the detector, from that calculated [37]

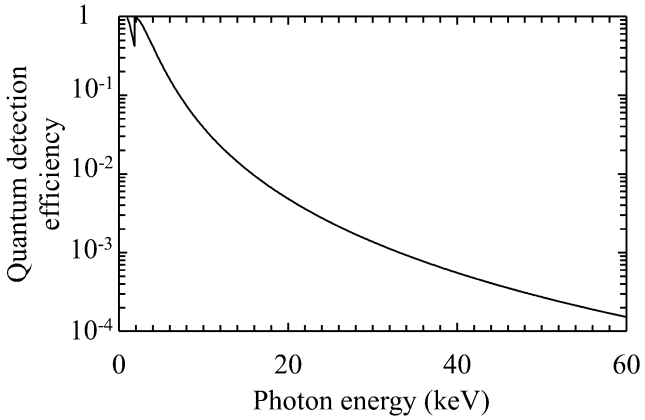

Fig. 3. Quantum detection efficiency of the SiC diode, reverse biased at 100 V. The discontinuity at 1.8 keV is the Si K absorption edge.

3.3 X/γ-ray Spectroscopy

The SiC photodiode was connected to a custom-built low-noise feedback resistorless charge-sensitive preamplifier (similar in design to that reported by reference [38]). The input transistor was a Vishay 2N4416A Si Junction Field Effect Transistor (JFET) [39]. Output signals from the preamplifier were shaped and amplified by an Ortec 572A shaping amplifier before being output to an 8k Ortec EASY multi-channel analyser (MCA). The detector bias was applied using a Keithley 6487 voltage source. Each radioisotope X-ray/γ-ray source (^{55}Fe, ^{109}Cd, ^{241}Am) was placed ≈ 9 mm above the detector in turn.

The test harness containing the SiC detector, preamplifier, and each radioisotope X-ray/γ-ray source, was located inside a TAS Micro MT climatic cabinet for temperature control. The other equipment was located outside of the climatic cabinet and operated at ambient laboratory temperature. The temperature inside the climatic cabinet was raised to 100 °C, and then decreased in 20 °C steps to 20 °C; spectra were accumulated at each set temperature. The process was repeated using each radioisotope X-ray/γ-ray source. All spectra were accumulated with the detector reverse biased at 100 V.

3.3.1 ^{55}Fe and ^{109}Cd X-ray spectroscopy

First, spectra were accumulated with an ^{55}Fe radioisotope X-ray source (activity 121 MBq). The spectra were accumulated at all available amplifier shaping times (τ = 0.5 μs, 1 μs, 2 μs, 3 μs, 6 μs, and 10 μs). The live time for each spectrum was 360 s. The photopeak detected from the ^{55}Fe radioisotope X-ray source was a combination of the characteristic Mn Kα (5.9 keV) and Mn Kβ (6.49 keV) ^{55}Fe X-ray emission lines [40]. Gaussians that took account of the relative emission ratios, and the relative detection efficiency of the SiC X-ray detector, were fitted to detected photopeaks to deconvolve the contributions of closely spaced X-ray emissions (e.g. Mn Kα and Kβ lines). The spectrometer was then calibrated using the position of the spectrometer's zero energy noise peak and a fitted X-ray peak (in this case the Mn Kα line), assuming a linear variation of charge with energy on the MCA's charge scale. A representative ^{55}Fe X-ray spectrum is presented in Fig. 4a. The counts of the zero energy noise peak in this spectrum were eliminated by setting the MCA low energy cut-off at ≈ 2.5 keV after determination of the zero energy noise peak's position. However, a small portion of the right hand side of the zero energy noise peak can still be seen. The total photocurrent collected by the SiC photodiode, calculated from the total counts in a spectrum was ~0.03 pA at all temperatures and shaping times. The energy resolution of the spectrometer (as quantified by the *FWHM* of the fitted Mn Kα photopeak) at the best available shaping time, as a function of temperature is shown in Fig. 5a. It should be noted here that the shaping time at 20 °C could be further optimized if the shaping amplifier had shaping times longer than 10 μs. The *FWHM* of the Mn Kα photopeaks improved from 2.69 keV ± 0.25 keV at 100 °C (at 1 μs shaping time) to 1.66 keV ± 0.15 keV at 20 °C (at 10 μs shaping time).

A second group of spectra were collected with the ^{55}Fe radioisotope X-ray source replaced with a ^{109}Cd radioisotope X-ray source (activity 296 MBq). Each ^{109}Cd spectrum had a live time of 2100 s. The same shaping times were used as for the ^{55}Fe X-ray measurements. The 88 keV γ-rays from the ^{109}Cd radioisotope source were not detected by the spectrometer because of the photodiode's low *QE* at 88 keV, the relatively low emission probability of that γ-ray, and the relatively short live time. A 0.23 mm PTFE attenuator, was placed between the ^{109}Cd radioisotope X-ray source and the detector to limit the photon count rate at lower energies where an Fe (Kα = 6.4 keV) fluorescence peak from the ^{109}Cd radioisotope source's capsule would have otherwise overshadowed the accumulated spectrum. The PTFE attenuated 0.730 and 0.038 of the fluorescent Fe Kα (6.4 keV) and ^{109}Cd Ag $K\alpha_1$ (22.16 keV) X-ray photons respectively. The characteristic

photopeaks detected from the ^{109}Cd radioisotope X-ray source were a combination of the five characteristic Ag Kα (21.99 keV and 22.16 keV) and Kβ (24.91 keV, 24.94 keV, and 25.45 keV) emission lines [41]. To measure the *FWHM* of the detected Ag $K\alpha_1$ (22.16 keV) peak, five Gaussians, were fitted to each accumulated spectrum. The spectrometer was calibrated in an analogous manner as for the ^{55}Fe X-ray spectra, using the fitted Ag $K\alpha_1$ (22.16 keV) emission peak. A representative ^{109}Cd X-ray spectrum accumulated with the spectrometer is presented in Fig. 4b. In this spectrum, the counts of the zero-energy noise peak were eliminated by setting the MCA low energy cut-off at ≈ 4 keV after determination of the position of the zero-energy noise peak as per the ^{55}Fe X-ray spectra. An Fe (Kα = 6.4 keV) X-ray fluorescence peak from the ^{109}Cd radioisotope X-ray source's capsule was still visible despite the inclusion of the attenuator to limit detection of such fluorescence photons. The low *QE* of the SiC detector at higher energy limited the photon count rate of the detector at higher energies. The average count rate in the Ag $K\alpha_1$ (22.16 keV) photopeak was 10.1 s^{-1} ± 0.2 s^{-1} and 9.2 s^{-1} ± 0.2 s^{-1} at 100 °C and 20 °C, respectively. The equivalent photocurrent created in the SiC photodiode, as calculated from the total counts in the detected ^{109}Cd spectrum was ≈ 0.009 pA, and was thus negligible as a steady state current noise source. The measured *FWHM* of the Ag $K\alpha_1$ photopeak, at the best available shaping time, as a function of temperature is shown in Fig. 5b. The *FWHM* of the Ag $K\alpha_1$ photopeak reduced from 2.65 keV ± 0.25 keV at 100 °C (at 1 µs shaping time) to 1.66 keV ± 0.15 keV at 20 °C (at 2 µs shaping time). The low energy tailing seen in Fig. 4 (e.g. as the saddle between the Ag Kα peak and the Fe Kα peak in Fig. 4b) was attributed to partial collection of charge created outside of the active region of the detector [42].

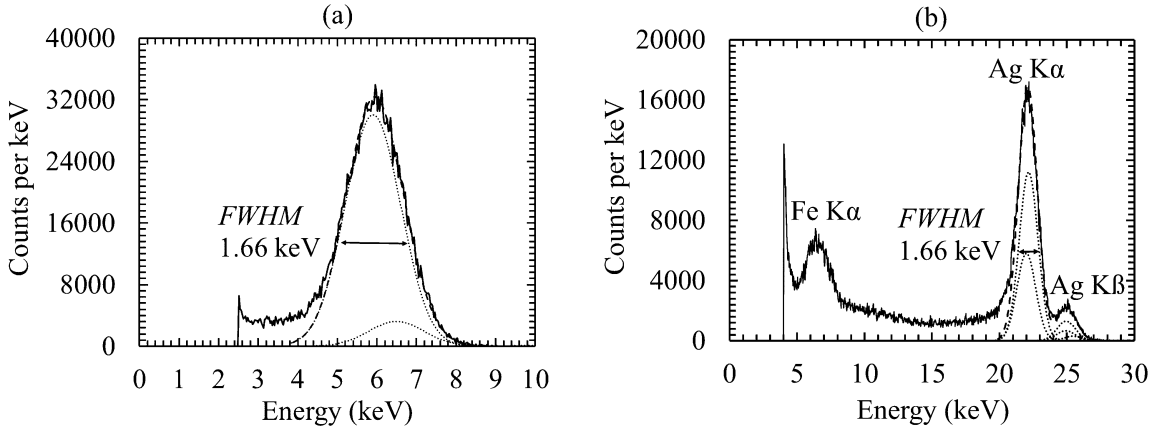

Fig. 4. Representative a) ^{55}Fe and b) ^{109}Cd X-ray spectra accumulated by the SiC spectrometer (solid line) at 20 °C, with the detector reverse biased at 100 V, and using 10 µs and 2 µs shaping times respectively. Dashed lines are the combined contributions fitted Gaussians; dotted lines are the respective Mn and Ag Kα and Kβ emission lines

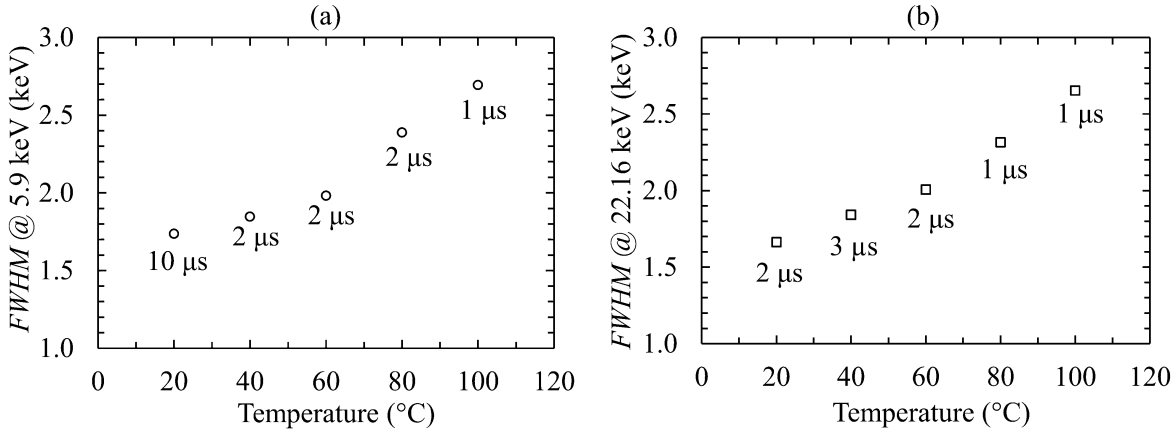

Fig. 5. *FWHM* of the fitted a) Mn Kα (5.9 keV) and b) Ag $K\alpha_1$ (22.16 keV) photopeaks, at the best available shaping time, as a function of temperature.

The shaping times that yielded the best (lowest) *FWHM* at 5.9 keV and 22.16 keV were similar within the uncertainties of measurements. As an example, at 20 °C the *FWHM* of the 5.9 keV photopeak was 1.66 keV ± 0.15 keV at 10 μs shaping time and 1.74 ± 0.15 keV at 2 μs shaping time. At the same temperature, the *FWHM* of the 22.16 keV photopeak was 1.74 keV ± 0.15 keV at 10 μs shaping time and 1.66 ± 0.15 keV at 2 μs shaping time. It was therefore useful to select the shaping times that produced the best *FWHM* at both energies to compare the performance of the spectrometer at 5.9 keV and 22.16 keV. The *FWHM* of the 5.9 keV and the 22.16 keV photopeak at identical shaping times are presented in Fig. 6.

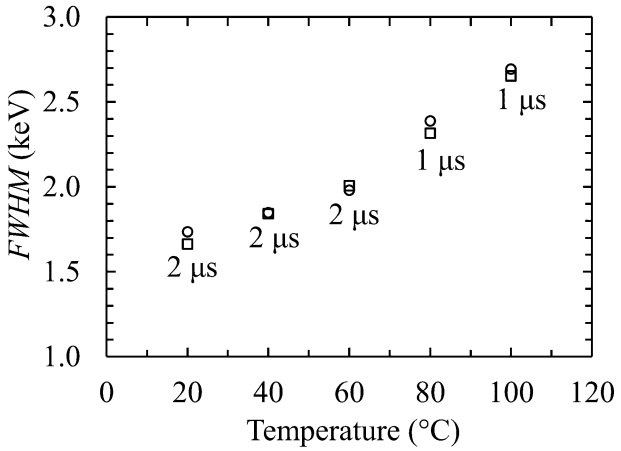

Fig. 6. *FWHM* of the Mn Kα (open circles) and the Ag $K\alpha_1$ (open squares) X-ray photopeaks as a function of temperature at the same amplifier shaping times.

The *FWHM* of the Mn Kα (5.9 keV) and the Ag $K\alpha_1$ (22.16 keV) photopeaks were 2.69 keV ± 0.25 keV and 2.65 keV ± 0.25 keV respectively at 100 °C and 1 μs shaping time; at 20 °C and 2 μs shaping time the *FWHM* reduced to 1.74 keV ± 0.15 keV and 1.66 keV ± 0.15 keV, respectively. The different noise components associated with the photopeaks' broadening are discussed in section 4.

3.3.2. ^{241}Am X-ray/γ-ray spectroscopy

The spectrometer was also investigated using an ^{241}Am X-ray/γ-ray source (activity 298 MBq) to illuminate the detector. The experimental set up and investigated temperature range for the ^{241}Am measurements was the same as was described for the ^{55}Fe and ^{109}Cd radioisotope X-ray source measurements. However, due to the lower quantum detection efficiency (1.56×10^{-4}) of the detector for the 59.5 keV γ-ray photons emitted by the ^{241}Am radioisotope γ-ray source, spectra were collected using only one shaping time at each investigated temperature. At temperatures ≥ 80 °C, spectra were accumulated at a shaping time of 1 μs; at temperatures < 80 °C, spectra were accumulated at a shaping time of 2 μs. Each spectrum had a live time of 6 days. Prior measurements were made to establish that the detector and preamplifier electronics were stable over durations of this length. To minimize disturbance to the detector and preamplifier front-end electronics, the PTFE attenuator mentioned in Section 3.3.1 was retained between the radioisotope radiation source and the detector; its attenuation of the 59.5 keV γ-rays was negligible (transmission = 0.991).

The spectrometer detected the characteristic ^{241}Am Np Lα (13.95 keV, 13.76 keV), Lβ (17.75 keV, 16.82 keV, 17.06 keV. 17.99 keV, and 17.51 keV), and Lγ, (20.78 keV, 21.10 keV and 21.34 keV) X-ray emissions as well as the two ^{241}Am γ-ray emission lines (26.34 keV and 59.54 keV) [41]. The sets of Np Lα, Lβ, and Lγ X-ray emissions formed three combined photopeaks since their individual components were not resolved by the spectrometer. Gaussians were fitted to the detected Np Lα, Np Lβ, ^{241}Am γ_1, and ^{241}Am

γ_2 photopeaks. The spectrum accumulated at 20 °C is presented in Fig. 7a. An Fe (Kα = 6.4 keV) fluorescence peak from the capsule of the ^{241}Am radioisotope X-ray/γ-ray source is also visible. The measured *FWHM* of the fitted Np Lα$_1$, Np Lβ$_1$, ^{241}Am γ_1, and ^{241}Am γ_2 peaks are shown as a function of temperature in Fig. 7b. The *FWHM* at 59.5 keV was 3.38 keV ± 0.30 keV at 100 °C (1 μs shaping time), this improved to 1.83 keV ± 0.15 keV at 20 °C (2 μs shaping time). The MCA's charge scale was calibrated using the position of the detected ^{241}Am γ_1 (59.5 keV) peak. At 20 °C, the Gaussian peak fitted to the ^{241}Am γ_1 photopeak contained a total of 23006 counts.

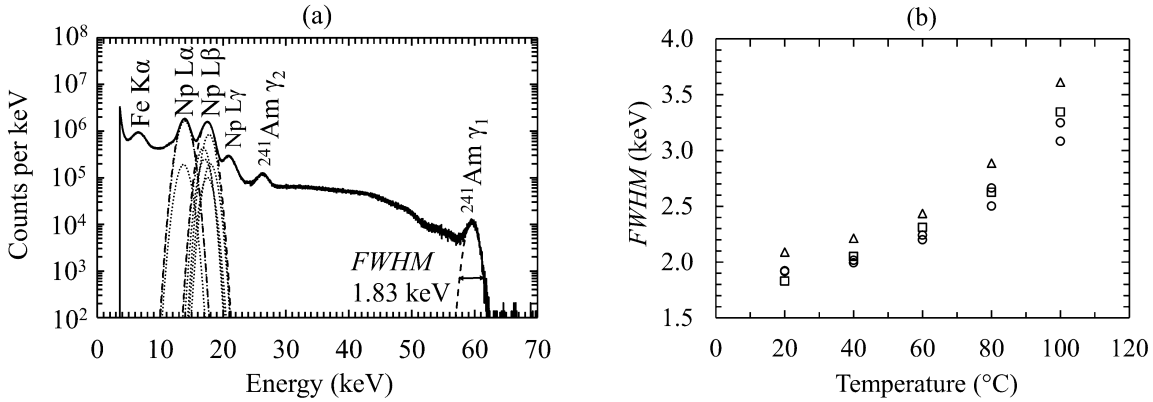

Fig. 7. a) ^{241}Am X-ray/γ-ray spectrum accumulated by the SiC spectrometer at 20 °C and using a 2 μs shaping time (solid line). Dashed lines are the combined contributions fitted Gaussians; the dotted lines are the Np Lα and Lβ emission lines respectively. b) Measured *FWHM* of the ^{241}Am Np Lα$_1$ (13.95 keV) (open triangles), Np Lβ$_1$ (17.75 keV) (open diamonds), ^{241}Am γ_2 (26.34 keV) (open circles) and ^{241}Am γ_1 (59.5 keV) (open squares) emission lines, at 1 μs (≥ 80 °C) and 2 μs (< 80 °C) shaping times, as a function of temperature.

4. Noise analysis and discussion

The noise in a direct detection (i.e. without scintillator) non-avalanche photodiode photon counting X-ray or γ-ray spectrometer is commonly considered to be separated into three independent contributions: Fano noise, which is related to the stochastic nature of the charge creation processes in the detector [43]; incomplete charge collection noise, which arises from any charge carrier trapping and recombination in the detector [44]; and electronic noise, which can be further separated into four components, white parallel noise, white series noise including induced gate current noise, 1/*f* series noise, and dielectric noise. For a review of these electronic noise components, the reader is directed to refs. [45, 46]. White parallel and white series noises vary with shaping time, whilst the other components are shaping time invariant. White parallel noise (driven by the total current at the input of the JFET) increases as shaping time is increased; white series noise (driven by the total capacitance at the input of the JFET) decreases as shaping time is increased.

The combined contribution of the shaping time invariant noise components and shaping time variant noise contributions were extracted from the *FWHM* measurements made at 5.9 keV (^{55}Fe Mn Kα) and 22.16 keV (^{109}Cd Ag Kα$_1$), as functions of shaping time, by performing multidimensional least squares fitting. Results of the multidimensional least squares fittings, at 20 °C and 80 °C, for the 5.9 keV data are presented in Fig. 8. At 100 °C there were an insufficient number of data points (shaping times) to conduct the multidimensional least squares fitting; only four shaping times were collected because of increased noise. The multidimensional least squares fittings for the Ag Kα$_1$ (22.16 keV) data at 20 °C, 80 °C, and 100 °C are presented in Fig. 9.

The best (narrowest) *FWHM* was achieved when the quadratic sum of white series and white parallel noise were a minimum. As an example, the best available shaping time to resolve the 5.9 keV (Mn Kα) photopeak

at 20 °C was 10 μs in the present system (Fig. 5a). The quadratic sum of white series noise and white parallel noise were a minimum at 10 μs shaping time (Fig 8a). For this X-ray energy (5.9 keV) and operating temperature (20 °C) the magnitude of the parallel white noise component was below the magnitude of the series white noise component at all the available shaping times.

In Figs. 8 and 9, Fano noise and *1/f* series noise were subtracted in quadrature from the combined shaping time invariant noise contributions, to show the quadratic sum of dielectric and incomplete charge collection noise.

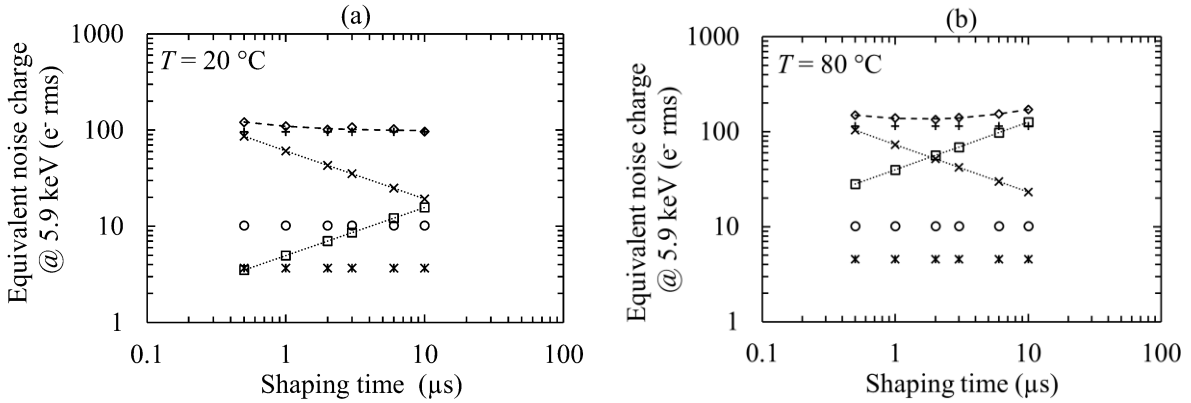

Fig. 8. *FWHM* and noise contributions as a function of amplifier shaping time of the ^{55}Fe 5.9 keV Mn Kα X-ray photopeak (open diamonds) at a) 20 °C and b) 80 °C. Quadratic sum of dielectric and incomplete charge collection noise (+ symbols), white parallel noise (open squares), white series noise (× symbols), Fano noise (open circles), *1/f* series noise (stars). Lines are a guide for the eye only.

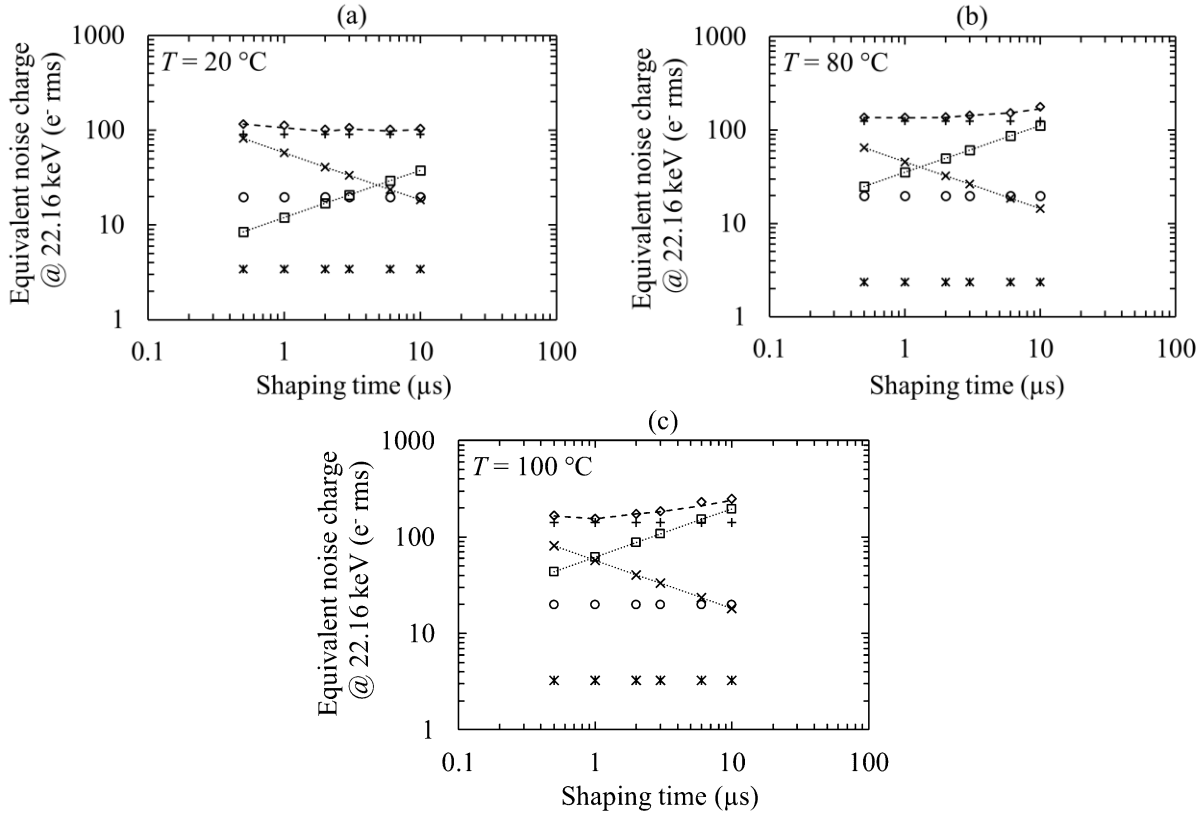

Fig. 9. *FWHM* and noise contributions as a function of amplifier shaping time of the ^{109}Cd 22.16 keV Ag $K\alpha_1$ X-ray photopeaks (open diamonds) at a) 20 °C, b) 80 °C, and c) 100 °C. Quadratic sum of combined dielectric and incomplete charge collection noise (+ symbols), white parallel noise (open squares), white

series noise (× symbols), Fano noise (open circles), 1/*f* series noise (stars). Lines are a guide for the eye only.

The Fano noise was calculated assuming a Fano factor of 0.128 and electron-hole pair creation energy of 7.28 eV [47]. Fano noise was calculated to be 10 e^- rms (175 eV *FWHM*), 20 e^- rms (338 eV *FWHM*), and 32 e^- rms (555 eV *FWHM*) at 5.9 keV, 22.16 keV, and 59.5 keV, respectively. 1/*f* series noise was calculated using the total capacitance at the input of the preamplifier derived from the multidimensional least squares fitting, with the capacitance of the preamplifier JFET estimated to be 2 pF [39, 45]. Comparison between the quadratic sum of dielectric and incomplete charge collection noise at two energies, in this case 5.9 keV and 22.16 keV, can be used to infer the presence or absence of incomplete charge collection noise in the spectroscopic system. The quadratic combination of dielectric and incomplete charge collection noise can be computed by subtraction in quadrature of the other (known) components outlined above. Since the total dielectric noise was unknown, incomplete charge collection noise could not be directly computed by subtraction (in quadrature) of dielectric noise. However, since dielectric noise is photon energy invariant and incomplete charge collection noise is known to be photon energy dependent [48] it was possible to determine if incomplete charge collection noise was significant by consideration of the spectrometer's response to different photon energies.

At 5.9 keV, the quadratic sum of dielectric and incomplete charge collection noise decreased from 115 e^- rms ± 3 e^- rms (1.97 keV) at 80 °C to 96 e^- rms ± 5 e^- rms (1.65 keV) at 20 °C. At 22.16 keV, the quadratic sum of dielectric and incomplete charge collection noise decreased from 125 e^- rms ± 3 e^- rms at 80 °C (2.14 keV) to 91 e^- rms ± 5 e^- rms (1.55 keV) at 20 °C. The reduction of dielectric noise with temperature is well documented [46, 49], but the specific quantitative reduction is impossible to predict without knowledge of the dielectric dissipation factors of each material contributing to the lossy dielectrics at the preamplifier's input. Although at each temperature, the quadratic sum of dielectric and incomplete charge collection noise, at each energy, were approximately equal, at 80 °C the difference (in quadrature) between dielectric noise and incomplete charge collection noise at 22.16 keV and 5.9 keV was significant (49 e^- rms ± 4 e^- rms). However, this difference in dielectric and incomplete charge collection noise between energies (5.9 keV and 22.16 keV) at 80 °C must be considered alongside other calculated noise contributions. For example, at 80 °C and at 1 µs shaping time the difference (in quadrature) of the white series noise at 5.9 keV and 22.16 keV was 57 e^- rms, and at longer shaping times similar differences in white parallel noise were recorded. Thus, it was not clear if any incomplete charge collection noise was present in the detector at 80 °C. Nevertheless, the dominant contributor to noise in the quadratic sum of dielectric and incomplete charge collection noise was dielectric noise.

The known components of the dielectric noise (those that are readily calculable) are the noise contributions from the SiC detector and the Si JFET, whilst the unknown dielectric noise contributions are the detector's packaging and feedback, stray and test capacitances of the preamplifier [49]. The unknown dielectric noise contributions are not easily estimated for lack of detailed knowledge of the dielectric dissipation factors and the dielectric constants of every source of capacitance within the preamplifier. The dielectric noise contribution from the SiC detector and the Si JFET can be estimated from capacitance measurements previously made on the SiC detector and attributing a nominal capacitance (2 pF [39]) to the Si JFET. The estimated dielectric noise contribution of the SiC detector and the Si JFET decreased from 5.6 e^- rms ± 0.3 e^- rms (10 eV) to 5.2 e^- rms ± 0.3 e^- rms (9 eV) and 28 e^- rms (460 eV) to 24 e^- rms (420 eV) from 80 °C to 20 °C respectively. Given that the dielectric noise contributions of the SiC detector and the Si JFET were low when compared with the quadratic sum of dielectric and incomplete charge collection noise calculated above there are opportunities to improve the resolution of the spectrometer by reducing or eliminating some of the stray capacitance (and the associated dielectric noise) acting at the input of the preamplifier. The preamplifier's JFET was packaged in a TO can, a simple noise reduction measure would be to re-locate the JFET and the detector onto a single package with the detector directly wire-bonded to the JFET. Furthermore, the preamplifier's PCB was FR4, replacing the FR4 board with a PTFE or ceramic

PCB would further reduce stray capacitance (and associated dielectric noise). A SiC JFET would also be beneficial [49].

White parallel noise (driven, in part, by leakage current) increased in magnitude at all shaping times as the temperature was raised, this was expected since the effect of increased temperature was to increase the leakage current of the packaged detector and the preamplifier's Si input JFET. As an example, considering the noise at 22.16 keV, the white parallel noise component at a shaping time of 1 μs increased from 12 e^- rms to 62 e^- rms from 20 °C to 100 °C respectively. The combined leakage currents of the SiC detector and Si JFET at the front of the preamplifier calculated from the linear least squares fittings is presented as a function of temperature in Fig. 10. The packaged detector's leakage current (section 3.1) was a small component of this total leakage current. The total leakage current in Fig. 10 represents the leakage current of the detector, the reverse biased JFET drain-to-gate junction current, and the forward biased JFET gate-to-source junction current. When all the different leakage currents are independent of each other, the total system leakage current is equal to twice the sum of the detector's leakage current and the JFET's drain-to-gate leakage current [12, 49]. The source of an n-type JFET such as that used in this preamplifier, is set to ground; consequently, the JFET's drain-to-gate leakage current was controlled by the drain-to-source and drain-to-gate potential differences. When the detector's leakage current decreased, the drain-to-gate voltage increased, which caused the drain-to-gate current to rise. This relationship between detector and JFET leakage current can be seen in the leakage current results shown in Fig. 2 and Fig. 10. At 80 °C, the detector's leakage current was 7.37 pA ± 0.42 pA at 100 V reverse bias, the corresponding leakage currents at the input to the preamplifier calculated from the multidimensional least squares fittings were 169 pA ± 18 pA and 136 pA ± 16 pA, when the SiC X-ray spectrometer was illuminated by the ^{55}Fe and ^{109}Cd radioisotope X-ray sources, respectively. At 60 °C, detector leakage current was 1.08 pA ± 0.40 pA, and the corresponding calculated leakage currents at the input to the preamplifier were 108 pA ± 11 pA, and 72 pA ± 19 pA for the same X-ray sources. When the detector's leakage current reduced, the leakage current from the JFET's drain-to-gate junction was a proportionately larger part of the total system leakage current.

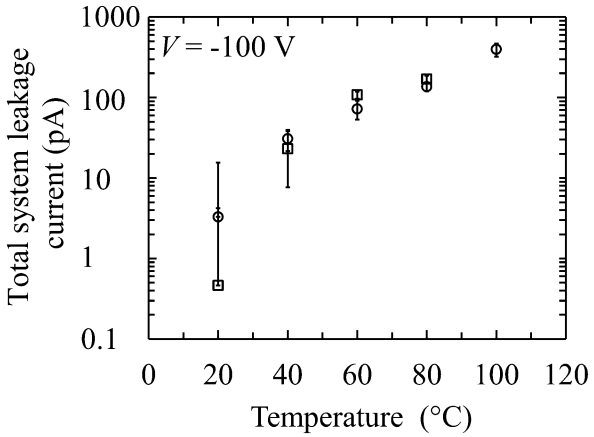

Fig. 10. The total leakage current contribution of the SiC diode and Vishay 2N4416A JFET (twice the sum of the detector's leakage current and the JFET's drain-to-gate leakage current) as a function of temperature as inferred from the multidimensional least squares fitting of the *FWHM* at 5.9 keV (open squares) and 22.16 keV (open circles) as a function of shaping time.

As the spectra collected with the ^{241}Am X-ray/γ-ray source were collected at a single shaping time multidimensional least squares fittings could not be conducted. Nevertheless, noise in the spectrometer at higher energy can be estimated from these results. The quadratic sum of electronic and incomplete charge collection noise was calculated by subtracting Fano noise in quadrature from the *FWHM* of the ^{241}Am 59.5 keV γ-ray peak at each temperature. The quadratic sum of electronic and incomplete charge collection noise from the ^{241}Am spectra were compared with the same noise contributions at 5.9 keV (^{55}Fe Kα) and

22.16 keV (^{109}Cd Kα_1), collected at the same shaping times. The results are presented in Fig. 11. The quadratic sum of electronic and incomplete charge collection noise at 5.9 keV, 22.16 keV and 59.5 keV were equal within the uncertainties ≥ 20 °C and ≤ 80 °C. This implied that incomplete charge collection noise, which is energy dependent, was negligible. However, at 100 °C the quadratic sum of electronic and incomplete charge collection noise at 59.5 keV exceeded that at 5.9 keV and 22.16 keV. As an example, at 20 °C, the quadratic sum of electronic and incomplete charge collection noise at 5.9 keV, 22.16 keV, and 59.5 keV was 103 e^- rms ± 9 e^- rms, 95 e^- rms ± 9 e^- rms, and 104 e^- rms ± 9 e^- rms respectively. At 100 °C the same noise contributions for the same energies were 157 e^- rms ± 15 e^- rms, 154 e^- rms ± 15 e^- rms and 192 e^- rms ± 18 e^- rms respectively, suggesting that some additional noise was present in the ^{241}Am (59.5 keV) photopeak. At 100 °C, the difference (in quadrature) between the quadratic sum of electronic and incomplete charge collection noise at 22.16 keV and 59.5 keV was 114 e^- rms ± 23 e^- rms. The additional noise could have been a consequence of greater than expected parallel white noise if the leakage current of the detector (or JFET) had been unstable when the reverse bias of the detector was held constant at 100 V for 6 days whilst the ^{241}Am spectrum was collected; as such, further measurements were made to investigate this. Incomplete charge collection noise was also considered a possible source of the extra noise, even though the higher temperature (100 °C) might have assisted in releasing trapped charge.

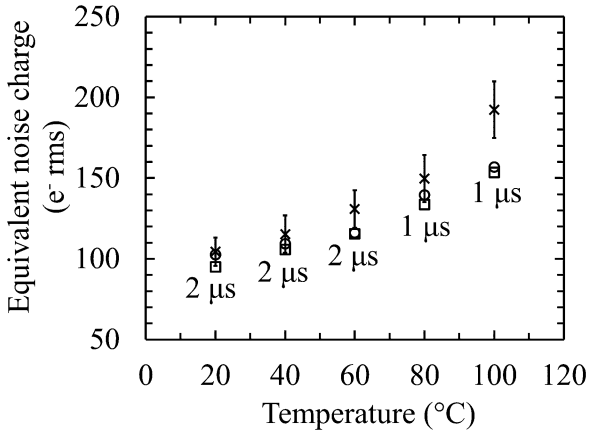

Fig. 11. Equivalent noise charge of the quadratic sum of electronic noise and incomplete charge collection noise as a function of temperature for the ^{241}Am 59.5 keV γ-ray photopeak (crosses), ^{109}Cd 22.16 keV X-ray photopeak (open squares), and the ^{55}Fe 5.9 keV X-ray photopeak (open circles). For clarity, only error bars for the ^{241}Am 59.5 keV γ-ray photopeak have been included. Errors bars for the ^{55}Fe Kα (5.9 keV) and ^{109}Cd Kα_1 (22.16 keV) X-ray photopeak ranged from 8.7 e^- rms to 14.6 e^- rms.

To test the long-term stability of the detector's leakage current, the detector was reversed biased for 6 days at 100 V and at 100 °C. The leakage current, which was measured at 60 second intervals using the procedures described in section 3.1, is presented in Fig. 12. At 100 V reverse bias the leakage current was initially 37.7 pA ± 0.5 pA, which was less than previously measured in section 3.1 (42.7 pA ± 0.5 pA). After 24 hours, the leakage current had risen to 47.5 pA ± 0.5 pA. After 48 hours the leakage current rose linearly at less than 0.01 pA per hour, whilst it oscillated 0.3 pA root mean squared (RMS) about an hourly mean value as it rose as a function of time. At the end of 6 days the leakage current was 49.0 pA ± 0.5 pA, the average leakage current over the final five hours of measurement was 49.1 pA ± 0.5 pA. Any leakage current rise in the detector should be considered in the context of its effect at the input to the preamplifier's JFET where the total system leakage current is equal to twice the sum of the detector's leakage current and the JFET's drain-to-gate leakage current (see previous paragraph). An extra leakage current of 22 pA at the input of the JFET would contribute ≈ 11 e^- rms noise broadening of the 59.5 keV γ-ray photopeak at 1 µs shaping time which was insufficient to account for all the extra noise. Therefore, the origin of the majority of the additional noise is currently unknown. Nevertheless, a significant contribution to the total invariant noise in the *FWHM* of the 59.5 keV γ-ray photopeak was dielectric noise.

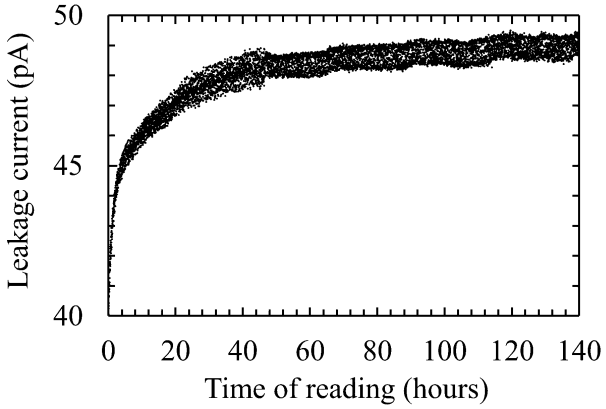

Fig 12. The packaged SiC detector's leakage current as a function of time, operating at 100 V reverse bias and at a temperature of 100 °C for 6 days.

These results achieved with a thin repurposed UV detector need to be viewed in context with some other wide bandgap compound semiconductor radiation detectors. This detector was thin (5.15 μm) and the detector's performance was modest compared with the best results for tailor-made detectors. A custom grown thick 4H-SiC strip X-ray detector depleted to a depth of 124 μm when reverse biased to 600 V has recently been reported [50]. This strip detector subsequently acquired an ^{241}Am spectrum at 200 V reverse bias with an ENC of 11.6 e^- rms (214 eV) at 21 °C. A 40 μm thick, 200 μm by 200 μm area pixel GaAs detector operating at 23 °C achieved a resolution of 266 eV (≈ 26 e^- rms) *FWHM* at 5.9 keV [51]. The results in refs [50, 51] were obtained from custom grown high quality materials attached to ultra-low noise preamplifier electronics and they benefitted from having the detectors directly wire bonded to the gate of the transistor at the front end of the preamplifier, rather than relying on discrete packaged transistors attached to the preamplifier's printed circuit board as was the case for the results reported here with a COTS SiC photodiode. Nevertheless, it is remarkable that the COTS SiC detector reported here, which was intended as a UV detector, functions as well as it does as a spectroscopic detector of X-rays and γ-rays up to 60 keV, and that it can operate continuously for up to 6 days, and at high temperature, without significant photopeak noise broadening caused by leakage current instabilities.

5. Conclusions and further work

A COTS 4H-SiC UV photodiode has been characterized for its electrical and photon counting spectroscopic response across the temperature, T, range 20 °C ≤ T ≤ 100 °C, and with X-ray and γ-ray photons in the energy range 5.9 keV to 59.5 keV.

The leakage current of the packaged SiC detector at 100 V reverse bias was found to be 42.7 pA ± 0.5 pA at 100 °C, and 1.1 pA ± 0.4 pA at 60 °C. At 40 °C and below the leakage current of the packaged SiC diode was below the noise floor of the picoammeter used (± 0.4 pA).

Measurements of capacitance as a function of reverse bias suggested that the detector could be depleted to 2.41 μm ± 0.03 μm at 20 °C, short of what was expected from the abrupt junction calculation [30] (3.7 μm at 100 V). Notwithstanding this, a previous electron spectroscopy study suggested that most of the epitaxial width (5.15 μm) was depleted and active [31]. It was also noted that carrier recombination lengths in the material were sufficiently large to address the difference in depletion width calculated from the capacitance - voltage measurements and the previous study that suggested the entire epitaxial thickness was active. Therefore, the *QE* of the detector was calculated using the full epitaxial width (5.15 μm) on the understanding that carriers were able either to diffuse to the depletion region prior to recombining or the full epitaxial width was depleted.

The detector was connected to a low noise charge sensitive preamplifier and operated as an X-ray / γ-ray spectrometer. The detector of the spectrometer was illuminated by ^{55}Fe, ^{109}Cd, and ^{241}Am radioisotope X-ray/ γ-ray sources and was found to be responsive to, and capable of discriminating (subject to its energy resolution) photons of energy up to 59.5 keV. The *FWHM* of a ^{55}Fe Mn Kα (5.9 keV) photopeak from a radioisotope source improved from 2.69 keV ± 0.25 keV at 100 °C to 1.66 keV ± 0.15 keV at 20 °C. A ^{109}Cd Ag $K\alpha_1$ (22.16 keV) photopeak likewise improved in *FWHM* from 2.65 keV ± 0.25 keV at 100 °C to 1.66 keV ± 0.15 keV at 20 °C. Following this, the spectrometer was operated continuously for 6 days at temperatures ranging from 100 °C to 20 °C, in 20°C decrements to accumulate ^{241}Am 59.5 keV γ-ray spectra. At 100 °C, the *FWHM* of the ^{241}Am 59.5 keV γ-ray photopeak was 3.38 keV ± 0.30 keV, which improved to 1.83 keV ± 0.15 keV at 20 °C.

The noise components degrading the spectrometer's energy resolution, beyond that which would be expected in the Fano limited case, were analyzed. A multidimensional least squares fitting of the measured *FWHM* as a function of shaping time for the accumulated ^{55}Fe and ^{109}Cd X-ray spectra showed that the dominant source of noise was dielectric noise at all the shaping times considered, up to temperatures of 40 °C. At higher temperatures (60 °C to 100 °C, inclusive), the combined currents of the SiC detector and the preamplifier's Si JFET increased white parallel noise to such an extent that white parallel noise became the dominant noise component at the longest shaping times (6 μs and 10 μs) at 100 °C. When the quadratic sums of electronic noise and incomplete charge collection noise were compared at 5.9 keV and 22.16 keV, incomplete charge collection noise was a negligible component of the total noise at lower temperatures (≤ 60 °C), at 80 °C the difference in quadrature of dielectric and incomplete charge collection noise at 5.9 keV and 22.16 keV was significant (≈ 49 e^- rms ± 4 e^- rms). At 59.5 keV and 100 °C, additional noise was also present. The detector's leakage current was measured again to determine if the detector was unstable when reverse biased for 6 days. Although the detector's leakage current rose by 11.3 pA ± 0.7 pA over the measurement period, this was insufficient to account for the broadening of the 59.5 keV ^{241}Am γ-ray photopeak which was observed. The source of the extra noise at 59.5 keV was unknown, but noise associated with incomplete charge collection at the higher energy could not be discounted.

The ready availability of these COTS devices, and the relative ease with which they can be repurposed from a UV photodiode to a uncooled spectroscopic soft and hard X-ray and γ-ray detector make them an attractive component for integration into an unshielded photon counting X-ray spectrometer on a low-cost low-mass CubeSat mission led by a University or a small entrepreneurial space-focused business. This COTS SiC radiation detector, could also find utility in terrestrial markets where the detector would be positioned uncooled, in a high radiation fluence background, without shielding, in difficult to access locations, and for extended periods. An oil well logging instrument being one example. The packaged detector and JFET would need to be appropriately paired with a commercial version of the low-noise charge sensitive preamplifier used in this test to minimize the dielectric losses that contributed to some of the photopeak broadening. Such an instrument, once built, would require further characterization and testing to determine its performance and optimum operating parameters and to identify definitively the source of the unknown noise component at 59.5 keV and 100 °C. Future work should include radiation damage testing, to investigate the radiation hardness of the detector and its degradation in performance over time when exposed to different types of high energy radiation.

Acknowledgements

This work was in part supported by the Science and Technologies Facilities Council, United Kingdom, through Grant No. ST/P002595/1. A.M.B acknowledges funding from the Leverhulme Trust, United Kingdom, in the form of a 2016 Philip Leverhulme Prize. C.S.B. acknowledges funding received in the form of a Ph.D. studentship from the Science and Technologies Facilities Council. The authors thank N.R. Gemmell for a MATLAB script used to automate the deconvolution of noise components. The authors thank M.D.C. Whitaker for LabVIEW scripts used to automate some measurements and for technical computing assistance with data processing.

Data Statement

Data underlying this work are subject to commercial confidentiality. The authors regret that they cannot grant public requests for further access to any data produced during the study, however the key findings are included within the article.

References

[1] W. Bludau, A. Onton, W. Heinke, Temperature dependence of the band gap of silicon, Journal of Applied Physics, 45 (1974) 1846–1848.

[2] G.W. Fraser, A.F. Abbey, A. Holland, K. McCarthy, A. Owens, A. Wells, The X-ray energy response of silicon Part A. Theory, Nuclear Instruments and Methods A, 350 (1994) 368–378.

[3] G. Bertuccio, Prospect for energy resolving X-ray imaging with compound semiconductor pixel detectors, Nuclear Instruments and Methods A, 546 (2005) 232–241.

[4] G.P. Summers, E.A. Burke, P. Shapiro, S.R. Messenger, R.J. Walters, Damage correlations in semiconductors exposed to gamma, electron and proton radiations, IEEE Transactions on Nuclear Science, 40 (1993) 1372–1379.

[5] B.M. Swinyard, K.H. Joy, B.J. Kellett, I.A. Crawford, M. Grande, C.J. Howe, V.A. Fernandes, O. Gasnault, D.J. Lawrence, S.S. Russell, M.A. Wieczorek, B.H. Foing, X-ray fluorescence observations of the moon by SMART-1/D-CIXS and the first detection of Ti Kα from the lunar surface, Planetary and Space Science 57 (2009) 744–750.

[6] A.M. Barnett, J.E. Lees, D.J. Bassford, J.S. Ng, C.H. Tan, N. Babazadeh, R.B. Gomes, The spectral resolution of high temperature GaAs photon counting soft X-ray photodiodes, Nuclear Instruments and Methods A, 654 (2011) 336–339.

[7] G. Bertuccio, D. Maiocchi, Electron-hole pair generation energy in gallium arsenide by x and γ photons, Journal of Applied Physics, 92 (2002) 1248–1255.

[8] Feng Zhang, Zhong He, G.F. Knoll, D.K. Wehe, J.E. Berry, 3-D position sensitive CdZnTe spectrometer performance using third generation VAS/TAT readout electronics, IEEE Transactions on Nuclear Science, 52 (2005) 2009–2016.

[9] P. Siffert, J. Berger, C. Scharager, A. Cornet, R. Stuck, R.O. Bell, H.B. Serreze, F.V. Wald, Polarization in Cadmium Telluride Nuclear Radiation Detectors, IEEE Transactions on Nuclear Science, 23 (1976) 159–170.

[10] A.M. Barnett, D.J. Bassford, J.E. Lees, J.S. Ng, C.H. Tan, J.P.R. David, Temperature dependence of AlGaAs soft X-ray detectors, Nuclear Instruments and Methods A, 621 (2010) 453–455.

[11] A.K. Saxena, Non-Γ Deep Levels and the Conduction Band Structure of $Ga_{1-x}Al_xAs$ Alloys, Physica Status Solidi B, 105 (1981) 777–787.

[12] G. Bertuccio, R. Casiraghi, Study of silicon carbide for X-ray detection and spectroscopy, IEEE Transactions on Nuclear Science, 50 (2003) 175–185.

[13] O. Madelung, Physics of Group IV Elements and III-V Compounds, Springer-Verlag, Berlin, 1982.

[14] F.J. Himpsel, J.A. Knapp, J.A. VanVechten, D.E. Eastman, Quantum photoyield of diamond(111)—A stable negative-affinity emitter, Physical Review B, 20 (1979) 624–627.

[15] C.J.H. Wort, R.S. Balmer, Diamond as an electronic material, Materials Today, 11 (2008) 22–28.

[16] D. T. Cromer and D. Liberman, Relativistic Calculation of Anomalous Scattering Factors for X-Rays, Journal of Chemical Physics, 53 (1970) 1891–1898.

[17] G. Bertuccio, R. Casiraghi, F. Nava, Epitaxial silicon carbide for X-ray detection, IEEE Transactions on Nuclear Science, 48 (2001) 232–233.

[18] G. Bertuccio, R. Casiraghi, A. Cetronio, C. Lanzieri, F. Nava, Silicon carbide for high resolution X-ray detectors operating up to 100°C, Nuclear Instruments and Methods A, 522 (2004) 413–419.

[19] G. Bertuccio, S. Caccia, D. Puglisi, D. Macera, Advances in silicon carbide X-ray detectors, Nuclear Instruments and Methods A, 652 (2011) 193–196.

[20] J. Lees, D. Bassford, A.M. Barnett, Lubricant analysis using X-ray fluorescence, US 2016/0202194A, 2016.

[21] G. Lioliou, A.M. Barnett, Prototype GaAs X-ray detector and preamplifier electronics for a deep seabed mineral XRF spectrometer, X-Ray Spectrometry, 47 (2017) 201–214.

[22] M. N Sweeting, C.I. Underwood, Spacecraft Systems Engineering, Fourth Edition, John Wiley and Sons Ltd, The Atrium, Southern Gate, Chichester, West Sussex, PO19 8SQ, United Kingdom, 2014.

[23] J.R. Terry, J.R. Distel, R.M. Kippen, R. Schirato, M.S. Wallace, Evaluation of COTS silicon carbide photodiodes for a radiation-hard, low-energy x-ray spectrometer, in: IEEE Nuclear Science Symposium Conference Record, Institute of Electrical and Electronics Engineers, (2011) 485–488.

[24] K.C. Mandal, P.G. Muzykov, J. Russell Terry, Highly sensitive x-ray detectors in the low-energy range on n-type 4H-SiC epitaxial layers, Applied Physics Letters, 101 (2012) 051111–4.

[25] K.C. Mandal, P.G. Muzykov, S.K. Chaudhuri, J.R. Terry, Low energy X-ray and γ-ray detectors fabricated on n-type 4H-SiC epitaxial layer, IEEE Transactions on Nuclear Science, 60 (2013) 2888–2893.

[26] S. Zhao, G. Lioliou, A.M. Barnett, Temperature dependence of commercial 4H-SiC UV Schottky photodiodes for X-ray detection and spectroscopy, Nuclear Instruments and Methods A, 859 (2017) 76–82.

[27] S. Zhao, T. Gohil, G. Lioliou, A.M. Barnett, Soft X-ray detection and photon counting spectroscopy with commercial 4H-SiC Schottky photodiodes, Nuclear Instruments and Methods A, 830 (2016) 1–5.

[28] S. Zhao, G. Lioliou, A.M. Barnett, X-ray spectrometer with a low-cost SiC photodiode, Nuclear Instruments and Methods A, 887 (2018) 138–143.

[29] D. Prasai, W. John, L. Weixelbaum, O. Krüger, G. Wagner, P. Sperfeld, S. Nowy, D. Friedrich, S. Winter, T. Weiss, Highly reliable silicon carbide photodiodes for visible-blind ultraviolet detector applications, Journal of Materials Research, 28 (2013) 33–37.

[30] S.M. Sze, K.K. Ng, Physics of semiconductor devices, John Wiley and Sons Ltd, Hoboken, NJ, USA, 2007.

[31] S. Zhao, G. Lioliou, S. Butera, M.D.C. Whitaker, A.M. Barnett, Electron spectroscopy with a commercial 4H-SiC photodiode, Nuclear Instruments and Methods A, 910 (2018) 35–40.

[32] G. Liaugaudas, D. Dargis, P. Kwasnicki, R. Arvinte, M. Zielinski, K. Jarašiunas, Determination of carrier lifetime and diffusion length in Al-doped 4H-SiC epilayers by time-resolved optical techniques, Journal of Physics D: Applied Physics, 48 (2015) 025103–10.

[33] V. Grivickas, J. Linnros, P. Grivickas, A. Galeckas, Band edge absorption, carrier recombination and transport measurements in 4H-SiC epilayers, Materials Science and Engineering B, 61–62 (1999) 197–201.

[34] G. Lioliou, X. Meng, J.S. Ng, A.M. Barnett, Characterization of gallium arsenide X-ray mesa p-i-n photodiodes at room temperature, Nuclear Instruments and Methods A, 813 (2016) 1–9.

[35] J.H. Hubbell, Review of photon interaction cross section data in the medical and biological context, Physics in Medicine and Biology, 44 (1999) R1–R22.

[36] M.J. Berger, J.H. Hubbell, S.M. Seltzer, J. Chang, J.S. Coursey, R. Sukumar, D.S. Zucker, K. Olsen, XCOM: Photon Cross Sections Database, (2010).

[37] G. Lioliou, M.C. Mazzillo, A. Sciuto, A.M. Barnett, Electrical and ultraviolet characterization of 4H-SiC Schottky photodiodes, Optics Express, 23 (2015) 21657–21670.

[38] G. Bertuccio, P. Rehak, D. Xi, A novel charge sensitive preamplifier without the feedback resistor, Nuclear Instruments and Methods A, 326 (1993) 71–76.

[39] Vishay Siliconix 2N4416/2N4416A/SST4416 N-Channel Silicon Junction Field-Effect Transistor, Document Number: 70242 S-04028 Rev. F, 2001, Fraunhoferstrasse 1A, 25524 Itzehoe, Germany.

[40] U. Schötzig, Half-life and X-ray emission probabilities of ^{55}Fe, Applied Radiation and Isotopes, 53 (2000) 469–472.

[41] S.Y.F. Chu, L.P. Ekström, R.B. Firestone, WWW Table of Radioactive Isotopes, Lund/LBNL Nuclear Data Search. (1996).

[42] A.M. Barnett, G. Lioliou, J.S. Ng, Characterization of room temperature AlGaAs soft X-ray mesa photodiodes, Nuclear Instruments and Methods A, 774 (2015) 29–33.

[43] U. Fano, Ionization Yield of Radiations. II. The Fluctuations of the Number of Ions, American Physical Society, 72 (1947) 26–29.

[44] A. Owens, Compound Semiconductor Radiation Detectors, Taylor & Francis Group LLC, Boca Raton, FL, USA, 2012.

[45] G. Bertuccio, A. Pullia, A method for the determination of the noise parameters in preamplifying systems for semiconductor radiation detectors, Review of Scientific Instruments, 64 (1993) 3294–3298.

[46] A.M. Barnett, J.E. Lees, D.J. Bassford, J.S. Ng, A varied shaping time noise analysis of $Al_{0.8}Ga_{0.2}As$ and GaAs soft X-ray photodiodes coupled to a low-noise charge sensitive preamplifier, Nuclear Instruments and Methods A, 673 (2012) 10–15.

[47] S.K. Chaudhuri, K.J. Zavalla, K.C. Mandal, Experimental determination of electron-hole pair creation energy in 4H-SiC epitaxial layer: An absolute calibration approach, Applied Physics Letters, 102 (2013) 31109–4.

[48] A. Owens, A. Peacock, Compound semiconductor radiation detectors, Nuclear Instruments and Methods A, 531 (2004) 18–37.

[49] G. Lioliou, A.M. Barnett, Electronic noise in charge sensitive preamplifiers for X-ray spectroscopy and the benefits of a SiC input JFET, Nuclear Instruments and Methods A, 801 (2015) 63–72.

[50] D. Puglisi, G. Bertuccio, Silicon Carbide Microstrip Radiation Detectors, Micromachines. 10 (2019) 835–847.

[51] A. Owens, M. Bavdaz, A. Peacock, A. Poelaert, H. Andersson, S. Nenonen, H. Sipila, L. Tröger, G. Bertuccio, High resolution X-ray spectroscopy using GaAs arrays, Journal of Applied Physics, 90 (2001) 5376–5381.